Experimental Thermal and Fluid Science 80 (2017) 228–243

Contents lists available at ScienceDirect

Experimental Thermal and Fluid Science

journal homepage: www.elsevier.com/locate/etfs

Flow characteristics of various three-dimensional rounded contour bumps in a Mach 1.3 freestream

Kin Hing Lo *, Konstantinos Kontis

Division of Aerospace Sciences, School of Engineering, University of Glasgow, University Avenue, Glasgow G12 8QQ, United Kingdom

ARTICLE INFO

Article history:
Received 18 May 2016
Received in revised form 23 August 2016
Accepted 29 August 2016
Available online 30 August 2016

Keywords:
Rounded contour bump
Supersonic wind tunnel
Flow control
Active blowing jet

ABSTRACT

Streamwise and spanwise flow pattern over three rounded contour bumps with different flow control strategies employed have been experimentally investigated in a Mach 1.3 freestream. Surface oil flow visualisation, Schlieren photography and particle image velocimetry measurements were used for flow diagnostics. Experimental data showed that in a Mach 1.3 freestream over the baseline plain bump, significant flow separation appeared at the bump crest that led to the formation of a large wake region downstream. In addition, two large counter-rotating spanwise vortices were formed in the bump valley. It was observed that the use of the passive by-pass blowing jet in the bump valley showed no obvious effects in reducing the sizes of both the wake region and the spanwise vortices in the bump valley. In contrast, it was found that the size of the wake region and the spanwise vortices could be reduced by blowing sonic jet in the bump valley. This approach of flow control found to be the most effective when the total pressure of the blowing jet was 2 bar. It is deduced that the active blowing jet hindered the formation of the spanwise vortices in the bump valley as well as deflected the shear layer downwards so that a smaller re-circulating bubble was formed downstream of the bump crest.

1. Introduction

In recent years, a number of studies have been conducted to investigate the potential of implementing rounded contour bumps into aerofoils or aircraft wings in attempt to achieve wave drag reduction in transonic aircraft [1–5]. It was estimated that about 5–15% of wave drag reduction could be achieved in a transonic aircraft with rounded contour bumps installed on to its wing surfaces [1–5]. Although promising results have been obtained from these studies, surprisingly, the underlying flow physics of rounded contour bumps is less well understood in both subsonic and supersonic flow regimes. Understanding the flow physics of rounded contour bumps is important as Konig et al. [2,3], Lo et al. [6], Bruce and Colliss [7] and Colliss et al. [8] have shown that unfavourable flow features like large spanwise counter-rotating vortices and three-dimensional vortical structures could form in the bump valley due to the appearance of flow separation at the bump crest. The presence of these unfavourable flow features and the occurrence of flow separation in the bump crest increase the pressure drag encountered by the contour bumps. Therefore, the drag reduction gained by installing contour bumps on to the wings could be partially or completely outweighed by the increase in the pressure drag encountered by the aircraft.

In subsonic flow, one of the earliest studies to investigate the flow physics of three-dimensional rounded contour bumps was conducted by Byun et al. [9]. The authors concluded that, in general, some large-scale three-dimensional vortical structures were observed downstream of the bump crest. In addition, spanwise, counter-rotating vortices were formed in the valley of the contour bumps. The authors indicated that the size and number of these spanwise vortex pairs that appear in the bump valley are functions of the length-to-width and length-to-height ratio of the rounded contour bumps [9]. Recently, Yakeno et al. [10] numerically investigated the problem of laminar flow over a two-dimensional rounded contour bump in subsonic freestream. The authors in [10] observed that the appearance of flow separation in the bump crest leads to the formation of large-scale three-dimensional vortical structures in the bump valley. In fact, similar vortical structures were also noticed by Iaccarino et al. [11] when a fully turbulent subsonic freestream was used. Moreover, the authors in [10,11] concluded that the size and shape of these vortical structures are flow Reynolds number dependent. In general, long and wide vortical structures were formed in laminar flow while shorter and narrower vortices appeared in turbulent flow.

* Corresponding author.
E-mail addresses: kinhing.lo@glasgow.ac.uk (K.H. Lo), kostas.kontis@glasgow.ac.uk (K. Kontis).

http://dx.doi.org/10.1016/j.expthermflusci.2016.08.027
0894-1777/

In supersonic flow regime, considerably limited data are available in the literatures to describe the physics of rounded-contour bump flow. The numerical study conducted by Svensson [12] was one of the studies to consider the streamwise and spanwise flow pattern over three-dimensional rounded contour bumps and their applicability in Diverterless Supersonic Inlets (DSI). Both subsonic and supersonic freestream were considered and a range of three-dimensional rounded contour bumps with different length-to-width and length-to-height ratios were used in this numerical study [12]. Similar to the findings mentioned in [6,9–11], the author in [12] observed that spanwise vortices were formed in the bump valley. Also, flow separation and hence, three-dimensional vortical structures were observed at the bump crest and the bump valley in nearly all bump geometries being studied [12]. The author concluded that for a three-dimensional rounded contour bump with a given width-to-apex height ratio, the sizes of the wake region that present downstream of the bump crest and the spanwise vortex pairs that formed in the bump valley increase with increasing the freestream Mach number (M_∞) in subsonic flow regime (i.e. $M_\infty < 1$). In contrast, the sizes of the spanwise vortices and the wake region decrease with increasing the freestream Mach number (M_∞) when the freestream is supersonic (i.e. $M_\infty > 1$) [12]. In fact, a similar conclusion was also drawn by Lo [13] when the author compared the flow pattern over a rounded contour bump in both Mach 1.3 and 1.9 freestream.

Lo [13] and Lo et al. [6,14] experimentally investigated the flow pattern over a three-dimensional rounded contour bump in a Mach 1.9 supersonic freestream. Experimental data shown in [6,13,14] confirmed the presence of the spanwise vortices and the wake region downstream of the bump crest as mentioned by Svensson in [12]. The authors in [14] proposed that the formation of the spanwise vortices was caused by the presence of the low pressure zones in the bump valley as a result of the flow separation. These low pressure zones attracted the flow around the bump from the two sides to move into and circulated in the bump valley that eventually led to the formation of the spanwise vortices. Interestingly, Lo [13] and Lo et al. [6,14] showed that the flow pattern downstream of the bump crest could be effectively altered by blowing sonic jet in the bump valley. The data shown in these studies [6,13,14] showed that the blowing sonic jet in the bump valley could effectively reduce the size of the wake region that presented downstream of the bump crest of a rounded contour bump. In addition, the blowing sonic jet also distorted and hindered the formation of the spanwise vortices in the bump valley. The authors in [14] concluded that this approach of flow control is particularly effective when high total pressure jet was used. In fact, similar effect of spanwise vortices distortion caused by injected jet in the leeward side of an object in supersonic freestream was also reported by Koike et al. [15], Zobkov et al. [16] and Kontis and Stollery [17] using a micro-ramp and a rounded flying object, respectively.

In should be noted that previous studies shown in [18–21] showed that wave drag reduction in airfoils, aircraft wings and inlet could be achieved by jet blowing alone in transonic freestream. However, using jet blowing alone in achieving wave drag reduction is not ideal as high volume of pressurised air is required for this purpose. This, in turn, means that significant amount of energy is required to drive the pump for generating pressurised air to achieve drag reduction in an airfoil or aircraft wing. In addition, to generate such a volume of compressed air required the use and installation of large-sized pumps and settling chambers in the aircraft. This significantly increases the weight of the aircraft and this explains why using active blowing jet alone is not an ideal solution to achieve wave drag reduction in transonic aircraft. The idea of combining rounded contour bump with active blowing jet (or combining micro-ramp with active blowing jet in the study conducted by Koike et al. [15]) seems to be able to provide an intermediate solution to this problem. This is because in this case the contour bumps (which is a passive flow control device and required no energy input) split the normal shock wave into a or a series of lambda shock wave structures on the wing surfaces in order to achieve wave drag reduction. The injected jet here is used to reduce the extent of flow separation that appears downstream of the bump crest so that maximum gain in drag reduction could be achieved. It is deduced that the volume of pressurised gas required in this case is considerably smaller than that required when using active blowing jet alone to achieve drag reduction on transonic aircraft wings.

The objectives of the present experimental studies have three folds. The primary objective is to extend the study conducted by Lo et al. [14] using a Mach 1.3 freestream in order to improve our understanding of the flow physics of three-dimensional rounded contour bumps in a lower supersonic speed. The Mach 1.3 freestream was used in order to simulate the flow conditions over the upper surface of the transonic aircraft wings. The second objective of this study is to investigate the effects of sonic jet blowing in suppressing the formation of the spanwise vortices in the bump valley as well as the wake region downstream of the bump crest of a three-dimensional rounded contour bump in a Mach 1.3 freestream. The data collected from this study are compared to those shown in [14] in order to investigate the similarity and discrepancy of the flow features that formed over the surface of the rounded contour bump in these two freestream speeds. The third objective of the present study is to introduce and investigate the flow pattern over a three-dimensional rounded contour bump with passive by-pass jet employed as the flow control strategy. It is clear in [6,14–16] that flow separation control could be effectively achieved by blowing active jet in the leeward side of a test model. However, it is unclear that could the same flow control effects also be provided by a passive jet, generated by diverting some flow from the windward to the leeward side of a bump. The data obtained in this study could assist the design of three-dimensional rounded contour bumps so that they could be successfully applied to transonic aircraft for the purpose of wave drag reduction.

2. Experimental setup

2.1. Supersonic wind tunnel

Experiments in the present study were conducted using an intermittent in-draft supersonic wind tunnel. A schematic of this wind tunnel facility is shown in Fig. 1 and the corresponding system diagram is presented in Fig. 2. The same wind tunnel was also used in a number of supersonic cavity [21–23] and contour bump flow related studies [6,13,14,25–27]. The wind tunnel has a rectangular-shaped test section with dimensions of 485.5 mm (length) × 150 mm (width) × 216 mm (height). Optical access is achieved through the two side windows and the ceiling mounted top windows. All of these windows are made of quartz.

The required Mach 1.3 supersonic freestream was generated by flow expansion through a pair of convergent-divergent nozzles situated upstream of the wind tunnel test section. The inlet of the supersonic wind tunnel is at atmospheric pressure. During wind tunnel operations, the static pressure (P) of the wind tunnel test section is P = 35.84 kPa and the corresponding static temperature (T) is T = 203.79 K. The flow Reynolds number per unit length (Re/L) is $Re/L = 12.11 \times 10^6$. The contour bump model was mounted on the floor along the centreline of the supersonic wind tunnel. It was situated at 82.5 mm downstream of the beginning of the wind tunnel test section. The wind tunnel has a stable run

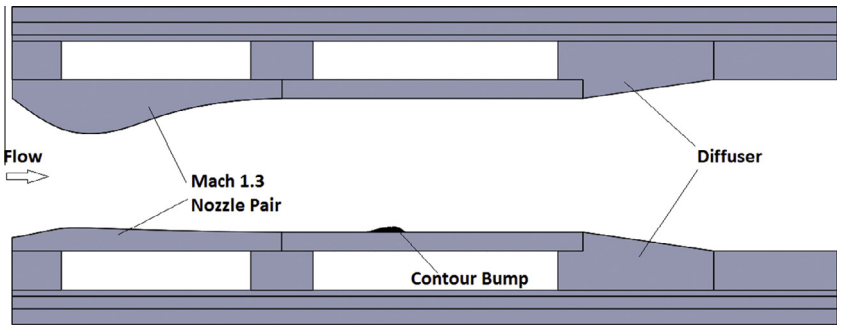

Fig. 1. Schematic of the supersonic wind tunnel used.

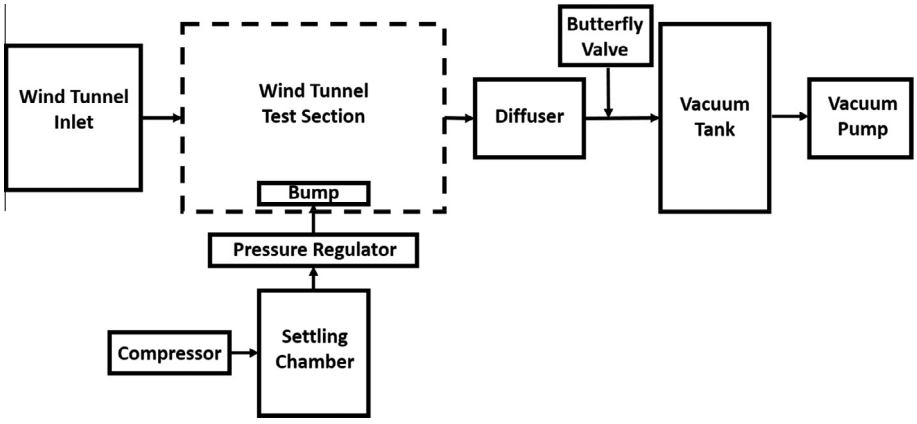

Fig. 2. System diagram of the supersonic wind tunnel used in the present study.

time of 6 s in a Mach 1.3 freestream. Under the same initial conditions, the variation of the freestream Mach number (M_∞) within the wind tunnel test section is about $M_\infty = 1.3 \pm 0.1$ [24].

The flow velocity profile in the wind tunnel test section measured at the location 5 mm upstream where the front end of the contour bump was situated is shown in Fig. 3.

The boundary layer profile measurement was conducted using a pitot rig which has ten pitot probes incorporated into it. The rear end of each pitot probe was connected to a Kulite XT-190M pressure transducer via a flexible tube. Voltage signals generated by the pressure transducers were captured by a National Instruments (NI) NI USB-6259 Data Acquisition (DAQ) system at a sampling rate of 20 kHz over a sampling period of 10 s. The measurement was repeated five times and the data collected were averaged for constructing Fig. 3.

From Fig. 3, it can be seen that the boundary layer thickness, calculated based on 99% freestream velocity (δ_{99}), is about $\delta_{99} = 14.9$ mm. This means that the contour bump models used in the present study were submerged in the boundary layer during the wind tunnel experiments. The corresponding displacement (δ^*) and momentum thickness (θ) of the boundary layer are $\delta^* = 4.54$ mm and $\theta = 2.57$ mm. This yields a shape factor (H), defined as $H = \delta^*/\theta$, of 1.77. Since the contour bump is submerged within the boundary layer of the incoming flow, the flow over the contour bump is not entirely supersonic. Based on the static temperature of 203.79 K in the wind tunnel test section, the speed of sound (a_∞) is equal to $a_\infty = 286\ ms^{-1}$. A sonic line which is situated at 7.6 mm above the floor level of the wind tunnel test section is shown in Fig. 3 to divide the flow into the subsonic and supersonic regions. To be exact, the incoming flow below the sonic line is subsonic and above which is supersonic.

2.2. Rounded contour bump models

In total, three rounded contour bump models, known as the plain bump, the passive jet bump and the active jet bump, were used. The geometry and dimensions of these contour bump models are identical. The dimensions of these contour bumps are 75 mm (length) × 50 mm (width) × 10 mm (crest height). The general geometry of these contour bump models is shown in Fig. 4. It should be noted that the same contour bump geometry was also employed by Qin et al. [4], Wong et al. [5] and very recently Lo et al. [14] and Zare-Behtash et al. [27].

Although these three rounded contour bump models have the same general geometry, different flow control strategies were incorporated into these models. The Computer Aided Design (CAD) models of the plain bump, the passive jet bump and the active jet bump are shown in Fig. 5(a)–(c), respectively. In the plain bump, no flow control device is incorporated into it as seen in Fig. 5 (a). In the passive jet bump (Fig. 5(b)), passive by-pass jet (i.e. diverting part of the flow from the front surface of the bump to the bump valley) is used as the flow control strategy. The front ramp-shaped surface and the valley of the passive jet bump are connected by three 1 mm diameter circular-shaped channels. These channels locate at 5 mm below the bump crest and one of these three channels is located along the centreline of the bump while the other two are located 3 mm away from the centreline at the two sides. Similar concept was applied to the active jet bump (Fig. 5(c)) although the continuous blowing jet in the bump valley was generated using compressed air. Three 2 mm diameter jet orifices, aligned at 45 degrees with respect to the transverse direction, are situated in the bump valley 5 mm below the bump crest. One of these three jet orifices is located at the centreline of the bump

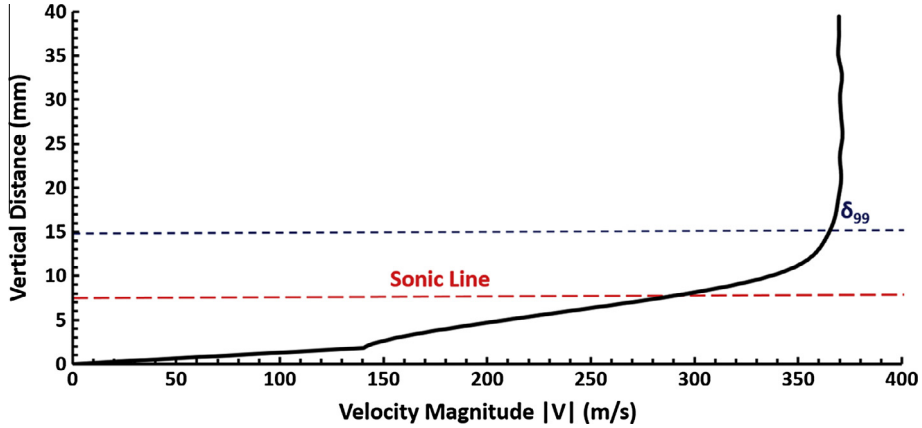

Fig. 3. Flow velocity profile measured at 5 mm upstream of the front end of the contour bump.

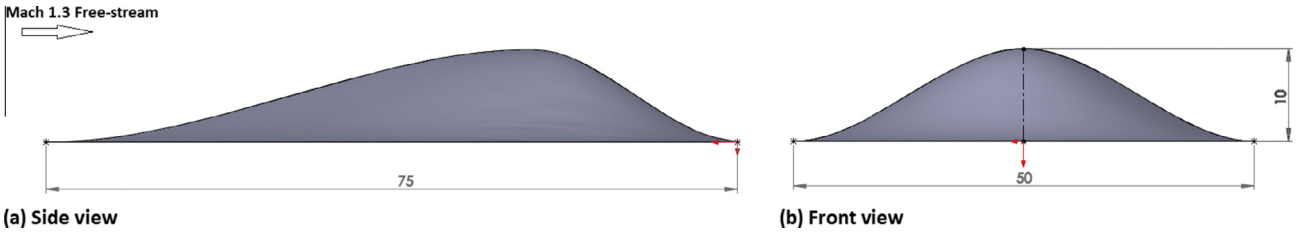

Fig. 4. General geometry of the rounded contour bump used. (a) Side view and (b) front view of the model.

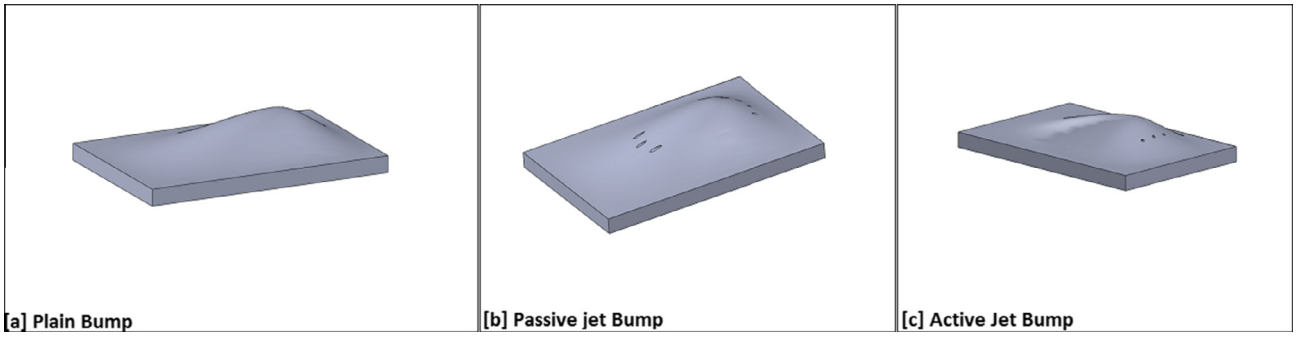

Fig. 5. Schematic of the three rounded contour bumps used. (a) Plain bump, (b) passive jet bump and (c) active jet bump.

while the other two are situated 3 mm away from the centreline at the two sides. Pressurised air with total pressure ranging from 0 (i.e. no jet) to 4 bar were injected into the cross-flow freestream through the three jet orifices. Since the outlets of these three jet orifices are converging and the static pressure inside the wind tunnel test section during the wind tunnel operation is around 0.36 bar, therefore, choked flow (i.e. sonic jet) is obtained at the outlets of the three jet orifices when the total pressure of the injected jet is set to 1 bar or above.

3. Flow diagnostics

3.1. Surface oil flow visualisation

Surface oil flow visualisation was used to examine the spanwise flow pattern over the surface of the three rounded contour bump models. The experimental setup used in the present study was identical to the set up employed in [6,13,14,26,28] and therefore, only a brief description is provided here. An in-house developed fluorescent oil was used as the dye in the surface oil flow visualisation experiments. It should be noted that same type of fluorescent oil was also used in [14,26]. This oil formulation has been proven to be able to follow the flow streaklines accurately in both Mach 1.3 and 1.9 supersonic freestream [14,26]. Three colours of fluorescent oil was used so that the effects of flow mixing in the flow field could be visualised easily. The fluorescent oil was applied 100 mm upstream of the front of the contour bump model using pipettes.

Uniform illumination to the wind tunnel test section was achieved using a pair of Ultra-Violet (UV) Light Emitting Diode (LED) panels place at the two sides of the wind tunnel test section. The same pair of UV LED panels was also employed in [14,23,29–37]. In order to increase the level of contrast, the contour bump models were first sprayed with five layers of matt black acyclic paint prior to the experiments. Instantaneous oil streaks left on the model surface was captured continuously during wind-on condition using a Cannon EOS600D Single Lens Reflection (SLR) camera. The camera was mounted on the ceiling of the wind tunnel test section. The shutter speed, ISO speed and the aperture size of the camera were set to 1/4000 s, ISO400 and F11, respectively.

3.2. High-speed monochrome Schlieren photography

Topler's z-type high-speed monochrome Schlieren photography technique was used to capture the streamwise flow pattern over the contour bump models in the Mach 1.3 freestream. It should be noted that the setup of the Schlieren system employed in this study was identical to the set up used in [14,26–29,38–40,41]. The high-speed Schlieren system used was composed of a 450 W continuous Xenon arc-lamp light source, manufactured by Newport (Model No.: 66924), a focusing lens, a 2 mm wide slit, a horizontal knife edge, a set of Hoya 49 mm diameter close-up lens, and a pair of parabolic mirrors. The diameter and focal length of each mirror are 203.2 mm and 2088 mm, respectively. A Photron FastCam SA1.1 monochrome high-speed camera was used to capture the streamwise flow pattern in the Schlieren photography experiments. The frame rate of the camera was set to 5000 frames per second with the corresponding resolution equal to 1024 pixels × 1024 pixels. In order to capture the unsteadiness effects in the flow field, the exposure time of the camera was set to 1 μs. The record time of the camera was about 2 s in each test and the images captured were stored in a Windows-based personal computer. It should be noted that in this study, the averaged shear layer and jet induced shock angles were measured and averaged from 200 instantaneous Schlieren images. The uncertainty of these angle measurements were quantified using statistical approach and tabulated in Table 1.

3.3. Two-component time-averaged particle image velocimetry (PIV) measurements

Time-averaged velocity information in the flow field was measured using the two-component Particle Image Velocimetry (PIV) technique. The experimental setup employed was identical to the setup shown in [14,23] and therefore, only a brief description is given here. The wind tunnel test section was illuminated by a Litron Nano L-series, Nd:YAG Model LPU550 Q-switched double-pulsed laser with maximum pulse energy output, repetition rate, laser pulse wavelength and pulse width of 200 mJ, 15 Hz, 532 nm and 4 ns, respectively. The laser beam was delivered to the ceiling of wind tunnel test section via a movable laser guide arm. A set of optics was mounted at the end of the laser guide arm to expand the laser beam into a thin laser sheet with thickness of approximately 0.8 mm. This thin laser sheet illuminated along the centreline of the wind tunnel test section. A time delay (Δt) of 0.8 μs between the two laser pulses (t) was used in the PIV experiments. It was calculated based on the analytically predicted freestream velocity of the Mach 1.3 freestream and the interrogation window size used in the PIV measurements. Through this arrangement, the seeder particle movement between two consecutive frames was 4 pixels.

Olive oil particles with density of 911 kg/m^3 and average particle size of 1 μm were used as the seeder particles. These particles were generated and delivered to the inlet of the supersonic wind tunnel by a TSI Model 9307 oil droplet generator with an aerosol flow rate of 30 L per minute. The Stokes number (Stk) of the seeder particles was Stk = 0.022 which ensured that the particles could follow the flow streamlines accurately. It should be noted that olive oil particles instead of solid seeder particles were used in the present study because of two safety related concerns. Firstly, the vacuum pump used for vacuuming the vacuum tank in this study could not handle solid particles. Therefore, potential mechanical damages to the vacuum pump may be induced if solid seeder particles are used in the PIV experiments. Secondly, the supersonic wind tunnel used in the present study has a considerably large test and inlet sections. Therefore, using solid seeder particles can lead to high concentration of solid powder being accumulated in both the inlet and the test section of the supersonic wind tunnel which can potentially causing the occurrence of dust explosion. Due to these two reasons, olive oil particles were used to replace solid particles as the seeder particles in the PIV measurement of the present study.

Table 1
Estimated uncertainty in the shear layer and jet induced shock angle measurements.

Measurements	Uncertainty
Shear layer angle	±1.0°
Jet induced shock angle	±1.5°

The scattered light from the seeder particles was captured by a LaVision Imager Pro X 2M CCD camera which viewed the laser sheet orthogonally. The camera used has a maximum resolution of 1600 pixels × 1200 pixels corresponding to a viewing area of 143 mm (length) × 107 mm (height). A Nikon 28–82 mm zoom lens was mounted on the camera and its aperture was set to F2.8. A 532 nm narrow band-pass filter was placed in front of the lens to minimise the background noise effects. The PIV measurements were repeated multiple times per contour bump model in order to ensure that the time-averaged vector field was constructed by averaging at least 300 pairs of images. The recorded images were stored in a Windows-based workstation and process through cross-correlation algorithm using the software Davis 7.2. The recorded images were first divided into a number of 64 pixels × 64 pixels (i.e. 5.7 mm × 5.7 mm) interrogation windows and two passes of cross-correlation were conducted. Afterwards, the interrogation window size was refined to 32 pixels × 32 pixels (i.e. 2.9 mm × 2.9 mm) and another three passes of cross-correlation were conducted. This multi-passes approach could improve the accuracy of the vector field that resolved through the cross-relation algorithm [14,23]. In addition, a 50% of overlapping between two neighbour interrogation windows was used for both stages of vector processing. This approach could reduce the number of spurious vectors appeared in the processed vector field [14,23].

Uncertainty of the PIV measurements was quantified using the method documented in Lusk [42] and Lusk et al. [43,44]. Noting that the Stokes number (Stk) of the seeder particles was Stk = 0.022 and the maximum turbulent intensity in the flow field was about 8% [13]. Since at least 600 images were used to construct the time-average vector field and using a 95% confidence interval, the corresponding overall uncertainty of the PIV measurements is 6.3%.

4. Results and discussion

4.1. Surface oil flow visualisation

The spanwise flow pattern along various contour bump models obtained from the surface oil flow visualisation experiments is shown in Fig. 6. The baseline spanwise flow pattern could be observed from Fig. 6(a) when the Mach 1.3 freestream is flown over the baseline plain bump. From Fig. 6(a) it can be seen that when the flow reached the front of the plain bump, the flow was deflected by the ramp-shaped front surface of the plain bump to move along and around the bump. The flow that moved along the front surface of the plain bump eventually reached the bump crest. A separation line (S.L.) is shown in the bump crest which indicates flow separation begins there. The occurrence of the flow separation is caused by the presence of an adverse pressure gradient where the subsonic flow decelerates continuously along the

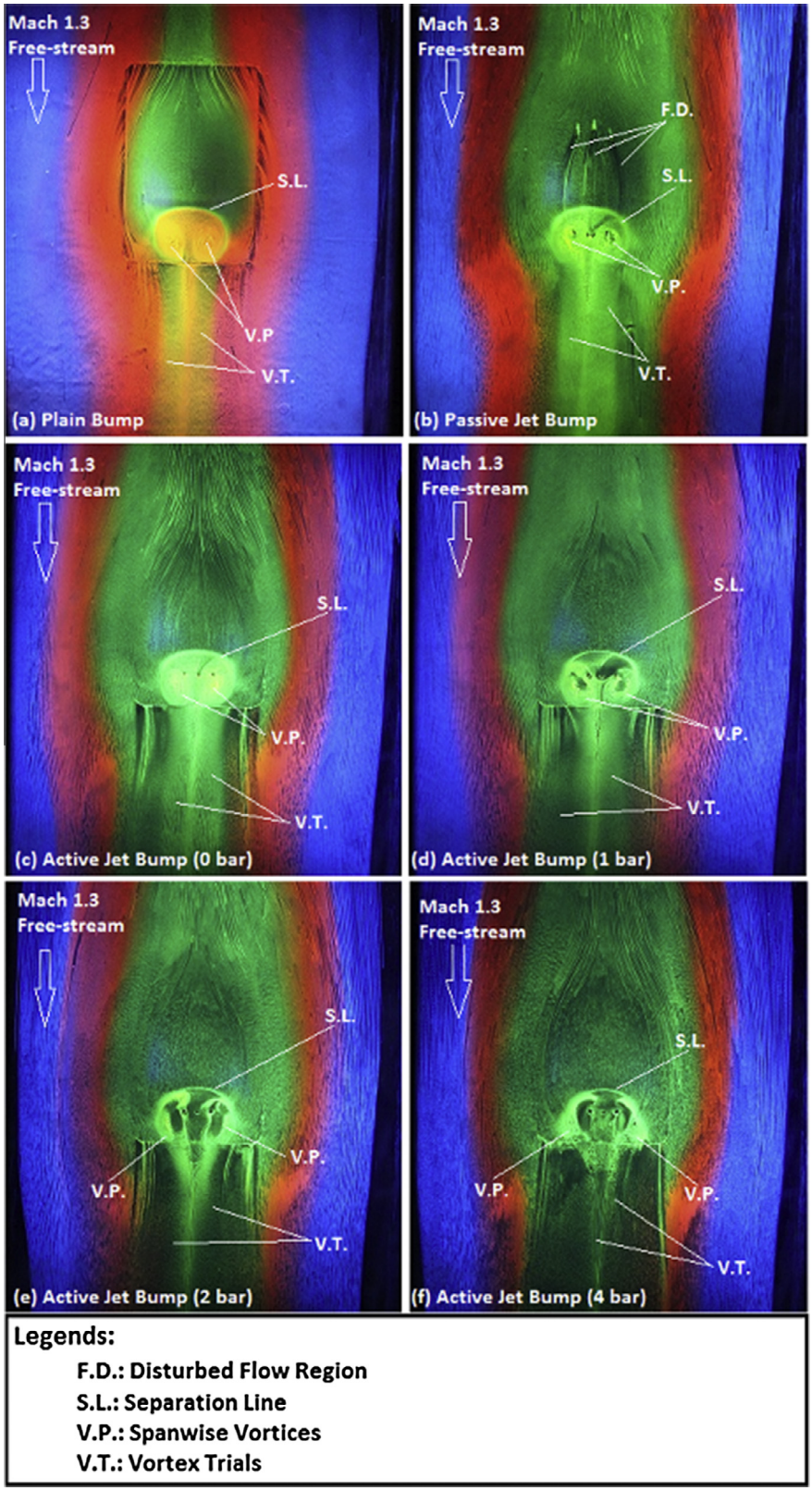

Fig. 6. Spanwise flow pattern along various contour bump models. (a) Plain bump, (b) passive jet bump and (c) to (f) active jet bump with 0 (i.e. no jet), 1, 2 and 4 bar total pressure sonic jet blowing in the bump valley, respectively.

bump valley [9]. As a result of the flow separation, a low pressure wake region is formed in the bump valley. This low pressure wake region attracts the flow from the two sides of the bump to move into and circulates in the bump valley. This is evidenced by the presence of the orange colour oil streaks in the bump valley which indicated that the flow moves along the bump (i.e. the green colour

oil streaks) is mixed with the flow from the two sides (i.e. the red[1] colour oil streaks) as seen in Fig. 6(a). The circulating flow in the bump valley leads to the formation of a large pair of counter-rotating spanwise vortices (V.P.). These spanwise vortices propagate downstream and hence, a pair of vortex trials (V.T.) is left behind the rear end of the plain bump.

Fig. 6(b) shows the spanwise flow pattern along the passive jet bump. Similar to the plain bump, the flow is deflected by the front surface of the bump to move along and sideways. However, from Fig. 6(b), it is clear that three thick lines (F.D.) appear in the middle of the ramp-shaped front surface of the passive jet bump. These oil-free regions are formed because of the three passive by-pass jet orifices that present at the bump front surface disturbs the incoming flow. Similar to the plain bump, a separation line (S.L.) appears at the bump crest of the passive jet bump which indicates flow separation begins there. However, the separation line that appears in the bump crest of the passive jet bump (Fig. 6(b)) is slightly thicker than that of the plain bump (Fig. 6(a)). This might indicate that flow separation begins slightly earlier in the passive jet bump than that occurs in the plain bump. Downstream of the bump crest, from Fig. 6(b), it can be seen that a pair of spanwise vortices is formed in the valley of the passive jet bump. Compare to the vortex pairs that appear in the valley of the plain bump (Fig. 6(a)) and the passive jet bump (Fig. 6(b)), it is clear that the size of these vortices is similar although the two vortices in the passive jet bump are more diffused. This implies that the flow that diverted from the front to the valley of the passive jet bump distorts the spanwise vortices in the bump valley. These spanwise vortices propagate downstream and therefore, a pair of vortex trial is left downstream of the passive jet bump.

In the case of the active jet bump with no jet is blowing in the bump valley (Fig. 6(c)), the general spanwise flow pattern along the bump is resemble to that along the plain bump (Fig. 6(a)). The size of the spanwise vortices (V.P.) and the width of the vortex trails (V.T.) in these two cases are similar. These indicate that the three jet orifices that present in the valley of the active jet bump did not induce any significant flow perturbation downstream of the bump crest. It should be noted here that the flow pattern shown in Fig. 6(c) is similar to the result shown in [14] when a Mach 1.9 supersonic freestream is used. However, the two spanwise vortices that formed in the bump valley in the present case (Fig. 6(c)) are larger than those shown in [14]. This finding is agreed with the conclusions drawn by Svenson [12] and Lo [13] about the effects of the freestream Mach number in affecting the spanwise flow pattern along various rounded contour bumps.

Changes start to appear when steady and continuous sonic jet is blowing in the valley of the active jet bump. Fig. 6(d) shows the spanwise flow pattern of the active jet bump with 1 bar total pressure jet blowing in the bump valley. From Fig. 6(d), it can be seen that the flow pattern upstream of the bump crest remains similar to that appears in the plain bump (Fig. 6(a)) and the active jet bump without jet blowing (Fig. 6(c)). A separation line (S.L.) is still presented at the bump crest although the thickness of the separation line in this case (Fig. 6(d)) is thinner than that of the plain bump (Fig. 6(a)). This indicates that the continuous blowing jet in the bump valley might exert certain effects in affecting the extent of flow separation downstream of the bump crest of the active jet bump. In the bump valley, from Fig. 6(d), it can be seen that two distorted spanwise vortices (V.P.) are formed. The size of these two vortices is slightly smaller than that of the plain bump (Fig. 6(a)). The appearance of smaller and more distorted spanwise vortices in the valley of the active jet bump in this case indicates that the continuous blowing jet hinders their formation. In fact, similar conclusion was also drawn by Lo et al. [14] using a Mach 1.9 freestream. Downstream of the rear end of the active jet bump, two vortex trails (V.T.) are shown in Fig. 6(d). However, the width of these two vortex trails is slightly narrower than those shown in the baseline plain bump. This indicates that the blowing jet in the bump valley not only reduces the size and strength of the spanwise vortices but also changing their propagation characteristics.

More dramatic changes occur downstream of the bump crest of the active jet bump when the blowing jet total pressure is increased to 2 bar. From Fig. 6(e), it can be seen that the two spanwise vortices (V.P.) that formed in the bump valley become highly diffused and their vortex cores cannot be located. In addition, the two spanwise vortices are much smaller in the present case compared to those shown in the valley of the plain bump (Fig. 6(a)). Moreover, in the present case (Fig. 6(e)), the two spanwise vortices in the bump valley moved upwards and towards the two sides of the bump valley due to the effects induced by the injected jet. In fact, similar vortex distortion and movement were also reported by Lo et al. [14] using a Mach 1.9 freestream although the flow features that shown in the bump valley in these two freestream speeds are considerably different. These differences are believed to be caused by various flow conditions in terms of the freestream Mach number and flow Reynolds number were employed in [14]. Similar to the case when 1 bar jet is blowing in the bump valley (Fig. 6(d)), a pair of vortex trails (V.T.) is left behind the rear end of the active jet bump in the present case. However, it can be clearly seen in Fig. 6(e) that these two vortex trails are much narrower than those shown behind the plain bump (Fig. 6(a)). This finding further confirms that the blowing jet in the bump valley could affect the propagation of the spanwise vortices downstream of the bump valley. Finally, when the total pressure of the blowing jet is increased to 4 bar (Fig. 6(f)) the spanwise flow pattern along the active jet bump remains similar to that when the jet total pressure is 2 bar (Fig. 6(e)). Interestingly, the two spanwise vortices (V.P.) that formed in the bump valley in the present case become slightly wider than those shown when 2 bar total pressure jet was used. However similar width of the vortex trails (V.T.) and thickness of the separation line (S.L.) are observed in these two cases.

To conclude, it is clear from previous discussion that the blowing jet in the bump valley could distort and reduce the size of the spanwise vortices that formed in the bump valley. These effects are particularly obvious when the total pressure of the jet is at 2 and 4 bar. It is deduced that the continuous blowing jet increases the pressure level locally around the centre portion of the bump valley. Therefore, a smaller low pressure zone is formed in the bump valley. As a result, less flow from the two side of the rounded contour bump could move and circulate in the bump valley when jet blowing is employed. Therefore, the resulting spanwise vortices that formed in the bump valley become smaller and more distorted. It is deduced that the area influenced by the blowing jet in the bump valley increases with increasing the total pressure of the injected jet. To be exact, the area that available for the formation of the spanwise vortices becomes progressively smaller when the total pressure of the blowing jet increases. This explains why, in general, the size of the spanwise vortex pair becomes progressively smaller with increasing jet total pressure of the injected jet in the valley of the active jet bump.

4.2. Schlieren photography

The streamwise flow pattern along various contour bump models being studied is shown in Fig. 7 in the form of Schlieren photography images. The baseline streamwise flow pattern over the plain bump is shown in Fig. 7(a). When the Mach 1.3 freestream reaches

[1] For interpretation of color in Fig. 6, the reader is referred to the web version of this article.

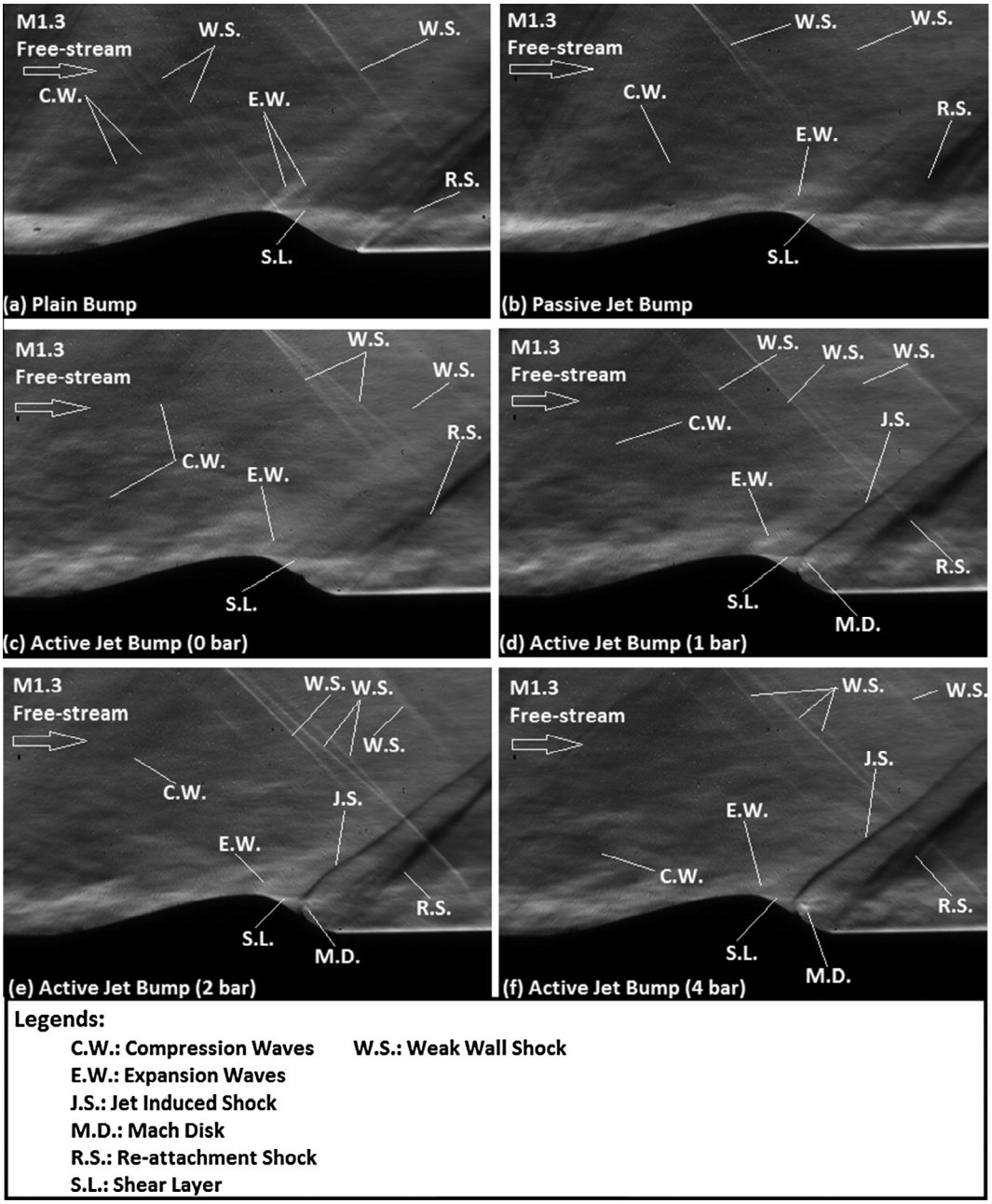

Fig. 7. Streamwise flow pattern along various contour bump models in the form of the Schlieren photography images. (a) Plain bump, (b) passive jet bump and (c) to (f) active jet bump with 0 (i.e. no jet), 1, 2 and 4 bar total pressure sonic jet blowing in the bump valley, respectively.

the front of the plain bump, a series of compression waves (C.W.) is formed at the beginning of the bump due to the flow compression effect induced by the ramp-shape front surface. From Fig. 7(a), it is clear that these compression waves are weak in strength as they could only barely be seen in the Schlieren image. Across the compression waves, the flow moves along the front face of the plain bump and reaches the bump crest. The flow is accelerated and expanded by a series of expansion waves (E.W.) that presented there. Therefore, a favourable pressure gradient is presented around the bump crest.

However, flow separation occurs downstream of the bump crest due to the rapid change in the bump geometry and the presence of an adverse pressure gradient along the bump valley. This is evidenced by the presence of a shear layer (S.L.) immediately downstream of the bump crest. The presence of the adverse pressure gradient along the bump valley is because the contour bump is submerged within the boundary layer. The flow in the boundary layer below 7.6 mm in height is subsonic as indicated in Fig. 3. Since the bump valley is concave in shape, the subsonic flow downstream of the bump crest is compressed and decelerated continuously along the valley of the plain bump. This results in the formation of an adverse pressure gradient along the bump valley and leads to the occurrence of flow separation [9]. Finally, at the rear end of the plain bump, the reattached shock (R.S.) appears and across which the flow becomes parallel to the freestream.

In addition to the flow structures and shock waves already mentioned, several weak shock waves known as the weak wall shock (W.S.) are emanating from the top wall of the wind tunnel test section. The formation of these shock waves was caused by the presence of some small gaps between the supersonic nozzle

situated upstream of the wind tunnel test section and the top window frame as well as between the top window and the window frame at the wind tunnel test section. Measures have been made in attempt to reduce the adverse effects caused by these small gaps although they could not be completely sealed. As a result, several weak wall shock waves were formed and emanating from the top wall of the wind tunnel test section. However, the strength of these wall shock waves is considerably weak. Therefore, it is believed that their existence should not induce significant effects in affecting the flow properties in the wind tunnel test section and could be ignored.

The streamwise flow pattern over the passive jet bump is shown in Fig. 7(b). From Fig. 7(b), it can be seen that the general streamwise flow pattern over the passive jet bump is similar to that shown over the plain bump (Fig. 7(a)), featured with the presence of the compression waves (C.W.) at the bump front as well as the expansion waves (E.W.) and shear layer (S.L.) at the bump crest. The only observable difference in the streamwise flow pattern between these two bumps is that the reattachment shock (R.S.) that formed at the rear end of the passive jet bump is weaker than that of the plain bump (Fig. 7(a)). In the case of the active jet bump with no jet blowing in the bump valley, the streamwise flow pattern over the bump as seen in Fig. 7(c) is very similar to that of the plain bump (Fig. 7(a)). This is expected as when no jet is blowing in the bump valley, the active jet bump is identical to the plain bump. Therefore, the flow pattern over these two contour bumps should be very similar which can be confirmed by observing the streamwise flow pattern over the plain bump and the active jet bump with no jet blowing in Fig. 7(a) and (c), respectively.

Changes in the streamwise flow pattern start to appear when the steady sonic jet is blowing in the valley of the active jet bump. When the blowing jet total pressure is 1 bar (Fig. 7(d)), upstream of the bump crest the flow features that presented remain similar to those shown in the plain bump (Fig. 7(a)). However at the bump crest, although the expansion waves (E.W.) and the shear layer (S.L.) are still presented there, it is clear that the shear layer is thinner in the active jet bump with 1 bar total pressure jet blowing compared to that shown in the baseline plain bump (Fig. 7(a)). In addition, from Fig. 7(d), it can be seen that the shear layer is pointing more downwards in the present case compared to the shear layer that shown in the plain bump (Fig. 7(a)) and the active jet bump without jet blowing (Fig. 7(c)). This finding indicates that the injected jet in the bump valley could deflect the shear layer downwards. To be exact, the blowing jet seems to exert effect in changing the size of the wake region that formed downstream of the bump crest. In fact, these findings can be proven when the PIV data are shown in the later Section 4.3. In the bump valley, an additional shock wave known as the jet induced shock (J.S.) can be observed from Fig. 7(d). This jet induced shock is formed immediately upstream of the three jet orifices in the bump valley and its formation is due to the ramping effect induced by the injected sonic jet. In addition, a Mach disk (M.D.) is presented immediately above the three jet orifices which can be seen from Fig. 7(d). This indicates that the injected jet is choked and hence, the jet velocity at the outlet of the orifices is sonic. In fact, similar flow features were also reported in [16–18] when a jet is continuously injected into a supersonic freestream. Finally, similar to all previous cases being studied, a reattachment shock (R.S.) appears at the rear end of the active bump which deflects the flow downstream to become parallel to the freestream.

Fig. 7(e) shows the streamwise flow pattern of the active jet bump with 2 bar total pressure jet blowing. Basically, the flow features that shown over the bump remain similar to those shown in the active jet bump with 1 bar total pressure jet blowing (Fig. 7(d)). However, from Fig. 7(e), it can be seen that the shear layer (S.L.) is pointing further downwards in the present case when 2 bar total pressure jet is used compared to that when the total pressure of the injected jet is 1 bar (Fig. 7(d)). This further indicated that the blowing sonic jet in the bump valley could deflect the shear layer downwards as well as implying that the shear layer angle changes with the total pressure of the injected jet. Downstream of the bump crest, a stronger jet induced shock (J.S.) and a more clearly defined Mach disk (M.D.) are shown in the valley of the active jet bump with 2 bar total pressure jet blowing (Fig. 7(e)) compared to those shown when the jet total pressure is 1 bar (Fig. 7(d)). The presence of the Mach disk suggests that the injected jet is choked and the jet velocity leaving the outlet of the jet orifices is sonic. Further increase in the total pressure of the injected jet from 2 to 4 bar does not cause significant changes in the flow pattern over the active jet bump. From Fig. 7(f), it can be seen that when the jet total pressure is 4 bar, the general flow pattern over the bump remains similar to that shown in Fig. 7(d) and (e) when the jet total pressure is 1 and 2 bar, respectively. The injected jet remains choked and the jet velocity at the jet orifices remains sonic. In the present case, the shear layer (S.L.) is pointing at an angle similar to that shown in Fig. 7(e) when the blowing jet pressure is 2 bar. However, in the bump valley, it can be seen that when 4 bar total pressure jet is used (Fig. 7(f)) the jet induced shock (J.S.) and the Mach disk (M.D.) that formed become more clearly defined than those shown when 1 (Fig. 7(d)) and 2 bar (Fig. 7(e)) total pressure jet are used.

Fig. 8 shows the relation between the averaged jet induced shock angle and the total pressure of the blowing jet measured and averaged from 200 instantaneous Schlieren photography images. It can be seen from Fig. 8 that the jet induced shock angle and therefore, the shock strength increases with increasing the total pressure of the blowing jet of the active jet bump. In fact a similar conclusion was also drawn by Ukai et al. [16]. It is deduced that the jet becomes progressively more under-expanded and hence, leads to the formation of progressively stronger jet induced shock when the total pressure of the blowing jet is increased.

There is one point should be noted here is that the jet induced shock angle shown in Fig. 8 indicates that the minimum jet induced shock angle appears in the case when 1 bar total pressure jet is injected into the freestream with the jet induced shock angle equal to 37.6°. Similarly, the maximum jet induced shock angle occurs when the total pressure of the injected jet is 4 bar and its angle is about 40°. These angles are apparently smaller than the Mach angle (μ) of a Mach 1.3 freestream (M_∞) which is equal to $\mu = 50°$. There are two possible reasons to account for the occurrence of this phenomenon. Firstly, the jet induced shock angles shown in Fig. 8 were measured with respect to the x-direction. However, downstream of the bump crest, the freestream is actually moving forwards and downwards. Therefore, the actual jet induced shock angle with respect to the flow direction downstream of the bump crest is larger than that angle shown in Fig. 8. Secondly, the jet induced shock angle smaller than the Mach angle of a Mach 1.3 freestream also suggests that the local flow Mach number above the boundary layer downstream of the bump crest (M_{valley}) is higher than Mach 1.3 (i.e. $M_{valley} > M_\infty > 1.3$). This is reasonable as expansion waves are presented around the bump crest of the contour bump as seen in Fig. 8. This means that the flow is expanded and accelerated along the bump crest and hence, the local flow velocity around the bump crest is higher than the upstream flow velocity. In addition, the flow expansion also reduces the local static temperature of the flow around the bump crest. In other words, the local speed of sound around the bump crest region is reduced. The presence of the higher local flow velocity and the lower local speed of sound around the bump crest indicate that the local flow Mach number (M_{valley}) is higher than Mach 1.3. This explains why the jet induced shock angle could be swallower than the Mach angle in a Mach 1.3 freestream.

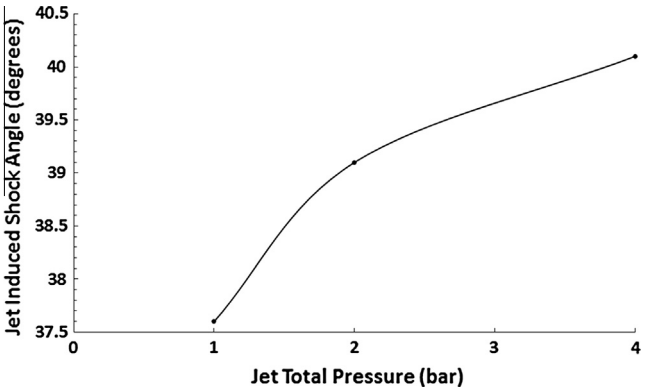

Fig. 8. Variation of the jet induced shock angle with the total pressure of the blowing jet.

In addition, as previously mentioned in this subsection that the blowing sonic jet seems to exert certain effects in changing the shear layer angle, this phenomenon could be quantitatively illustrated by measuring the averaged shear layer angle with respect to the freestream direction of all contour bumps being studied. The results of measurements obtained are shown in Fig. 9. It should be noted that the averaged shear layer angles shown in Fig. 9 are obtained by averaging 200 instantaneous Schlieren images for each test case being studied.

From Fig. 9, it can be seen that the shear layer angle of the plain bump, the passive jet bump and the active jet bump with no jet blowing in the bump valley are similar which can be revealed by observing the Schlieren images shown in Fig. 7(a)–(c) for these three cases. The shear layer angle of the passive jet bump in fact is marginally larger than that of the plain bump as shown in Fig. 9. This indicates that the shear layer in the passive jet bump points less downwards compared to the plain bump. Significant changes in term of the shear layer angle appear when active jet is blowing in the valley of the active jet bump. In general, from Fig. 9, it can be seen that the shear layer angle decreases (i.e. the shear layer points more downwards) with increasing the total pressure of the blowing jet although the shear layer angle in fact is marginally larger in the case when the jet total pressure is 4 bar than when it is 2 bar. The data shown in Fig. 9 further indicated that the blowing sonic jet in the valley of the active jet bump could deflect the shear layer downwards. In addition, these data also confirmed that the shear layer angle is influenced by the total pressure of the injected jet of the active jet bump.

4.3. Two-component particle image velocimetry measurements

After showing the streamwise flow pattern over various rounded contour bump being studied in the form of Schlieren images, their corresponding velocity information measured from the time-average two-component PIV measurements is presented in this subsection. The time-averaged x-velocity contours along the centreline of various rounded contour bumps being studied are first shown in Fig. 10. In general, the x-velocity contours upstream of the bump crest for all rounded contour bumps being studied are similar as seen in Fig. 10. Since the compression waves that formed at the front end of these rounded contour bumps are weak in strength, therefore no significant x-velocity reduction could be observed in Fig. 10(a)–(f) in all contour bumps being studied. Near the bump crest of the plain bump (Fig. 10(a)), passive jet bump (Fig. 10(b)) and the active jet bump without jet blowing (Fig. 10(c)), a region which shows relatively high x-velocity appears due to the flow expansion effect caused by the expansion waves that presented there. This indicates that a favourable pressure gradient is presented around the bump crest (i.e. the region between $x/h > 5$ and $y/h > 0.76$). To be exact, the flow remains attached immediately downstream of the bump crest (i.e. $x/H > 5$ and $0.76 < y/H < 1$) due to the presence of this favourable pressure gradient. In those cases of the active jet bump with jet blowing in the bump valley as seen in Fig. 10(d)–(f), the flow expansion leads to the occurrence of a region that shows considerably high x-velocity at and immediately downstream of the bump crest. However, immediately downstream of the first flow expansion region, a small region that shows abrupt x-velocity reduction appears which can be seen clearly from Fig. 10(d)–(f) when the total pressure of the injected jet is 1, 2 and 4 bar, respectively. The occurrence of this abrupt x-velocity reduction is caused by the jet induced shock. It is interested to note that, from Fig. 10(d)–(f), it can be seen that the size of this relatively low x-velocity region remains similar when the blowing jet total pressure is progressively increased from 1 to 4 bar. Behind this low x-velocity region, the flow is expanded and accelerated again and therefore, a second region of relatively high x-velocity appears in the bump valley which can be seen in Fig. 10(d)–(f) when 1, 2 and 4 bar total pressure jet is injected in the valley of the active jet bump, respectively.

Completely different flow pattern is shown in and immediately downstream of the bump valley of these rounded contour bumps. For the plain bump (Fig. 10(a)), due to the occurrence of flow separation at the bump crest, a big recirculating flow region or the wake region is formed in the bump valley. As already mentioned, the flow along most part of the bump valley is subsonic (i.e. the region between $x/h > 5$ and $y/H < 0.76$). Therefore, the flow decelerates along the concave shaped bump valley and therefore, an adverse pressure gradient exists. The presence of this adverse pressure gradient leads to the occurrence of the flow separation and the formation of the wake region downstream of the bump crest [9]. Quantitatively, the normalised length and height of the wake region of the plain bump are about 0.27 c and 0.093 c, respectively. It should be noted that c is the length of the contour bump which is 75 mm. In addition, qualitatively, it can be seen from Fig. 10(a) that strong reverse flow appears in the wake region which indicates that flow recirculation within the wake region of the plain bump is considerably strong. Similar flow pattern appears in the valley of the passive jet bump shown in Fig. 10(b). A considerably large wake region is formed downstream of the bump crest of the passive jet bump and its normalised length and height are 0.27 c and 0.1 c, respectively. In other words, the size of the wake region of the passive jet bump is marginally larger than that shown in the plain bump. However, qualitatively, weaker reverse flow appears in the wake region of the passive jet bump (Fig. 10(b)) compared to that of the plain bump (Fig. 10(a)). This implied that although the size of the wake region could not be reduced by using passive by-pass jet in the bump valley, the passive jet could weaken the recirculating flow in the wake region.

In the case of the active jet bump without jet blowing (Fig. 10(c)), the size and strength of the reverse flow in the wake region is similar to those shown in the wake region of the plain bump (Fig. 10(a)). In fact, in this case, the normalised length and height of the wake region are 0.27 c and 0.094 c, respectively which are almost identical to the size of the wake region of the plain bump. This is expected as the active jet bump could be treated as a plain bump when no jet is blowing in the bump valley. Changes start to appear in the wake region when continuous jet is blowing in the valley of the active jet bump. In the case when the jet total pressure is 1 bar (Fig. 10(d)), qualitatively, it can be seen from Fig. 10(d) that the size of the wake region remains similar to that shown in the plain bump (Fig. 10(a)) and the active jet bump without jet blowing (Fig. 10(c)). Quantitatively, the normalised length and height of the wake region in this case are 0.27 c and 0.09 c, respectively.

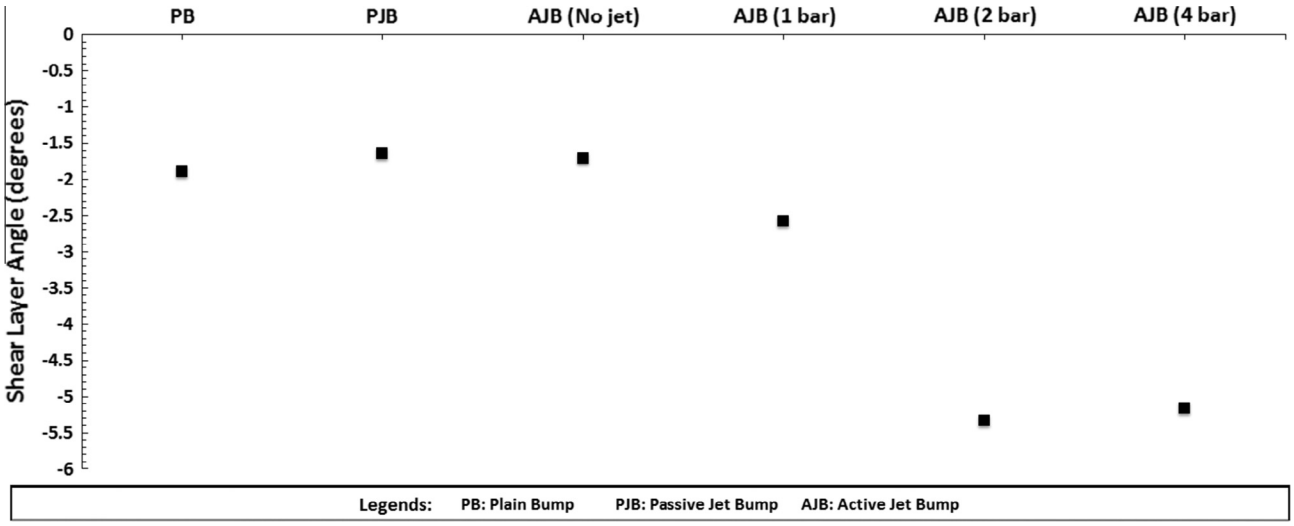

Fig. 9. Shear layer angle of various rounded contour bumps being studied.

These values are comparable to the wake region sizes of the plain bump and the active jet bump without jet blowing. Although the 1 bar blowing jet of the active jet bump seems unable to reduce the wake size, it can be seen from Fig. 10(d) that the strength of the reverse flow in the wake region is significantly reduced. This indicated that the blowing jet in the bump valley could reduce the strength of the recirculating flow that presented in the wake region.

Dramatic changes appear in the active jet bump when the blowing jet total pressure is 2 bar (Fig. 10(e)). In this case, the size of the re-circulating flow region in the bump valley becomes significantly smaller than that shown in the active jet bump without jet blowing (Fig. 10(c)) and when the jet total pressure is 1 bar (Fig. 10(d)). Quantitatively, the normalised length and height of the wake region in this case are 0.14 c and 0.004 c, respectively. This means that compared to the wake region of the plain bump, the recirculating flow region of the active jet bump with 2 bar total pressure jet blowing in the bump valley is approximately 77% smaller. In addition, basically no reverse flow appears in the wake region in this case when 2 bar total pressure jet is blowing in the bump valley (Fig. 10(e)). In fact, similar phenomena could also be observed in the active jet bump when the jet total pressure is increased to 4 bar. From Fig. 10(f), similar to the case when the total pressure of the injected jet is 2 bar, nearly no reverse flow is shown in the wake region of the bump. However, it is interested to note here that the size of the wake region in this case (i.e. 4 bar total pressure jet blowing in the bump valley) is slightly larger than that when 2 bar total pressure jet is injected. Quantitatively, the normalised length and height of the wake region in the present case are 0.18 c and 0.08 c, respectively. Therefore, the size of the wake region in this case when 4 bar total pressure jet is used is about 42% smaller than that of the plain bump (Fig. 10(a)) and the active jet bump without jet blowing (Fig. 10(c)). The data obtained from the PIV measurements for the active jet bump with 2 and 4 bar total pressure jet blowing indicate that the continuous blowing jet could effectively reduce the size and the strength of the recirculating flow region that presented in the valley of the rounded contour bumps.

In fact, the flow characteristics in the wake region of all contour bumps being studied could be further investigated by plotting the x-velocity profiles at various normalised x-locations (x/h) ranging from $6 < x/h < 9$ along the wake region of the bumps and the plot is shown in Fig. 11. It should be noted that the variable h in Fig. 11 is the apex bump height which is 10 mm. There are several trends regarding the size and strength of the wake region could be observed from Fig. 11(a)–(d). Firstly, the wake region of the active jet bump with 2 and 4 bar total pressure jet blowing in the bump valley is much narrower than any other rounded contour bump being studied. This can be revealed from Fig. 11(a)–(d) that the regions which show negative or low x-velocity in these two cases are always smaller than any other contour bumps being studied. Secondly, in terms of the strength of the wake region, from Fig. 11(a)–(d), it can be seen that in the region between $6 < x/h < 9$ the x-velocity of the flow is always higher in the cases when 2 and 4 bar total pressure jet is blowing in the valley of the active jet bump than that of any other contour bumps being studied. In fact, it can be seen that at the normalised x-locations $x/h = 6$ (Fig. 11(a)) and $x/h = 7$ (Fig. 11(b)) the strongest reverse flow appears in the wake region (i.e. the region between $0 < y/h < 0.76$) of the plain bump, followed by the active jet bump without jet blowing. These results confirmed that considerably strong wake regions are formed downstream of the bump crest in these two bumps.

In contrast, the reverse flow that appears in the wake region of the passive jet bump and the active jet bump with jet blowing in the bump valley is always weaker than that shown in the plain bump and the active jet bump without jet blowing. In fact, from Fig. 11(a), it is clear that at the normalised x-location $x/h = 6$, the x-velocity in the wake region, i.e. the region between $0 < y/h < 0.8$, is the highest when 2 bar total pressure jet is blowing, followed by 4 and 1 bar total pressure jet blowing in the valley of the active jet bump. It is interested to note here that at the normalised x-location $x/h = 6$ (Fig. 11(a)), the x-velocity in the wake region of the passive jet bump is slightly higher than that of the active jet bump with 1 bar jet blowing in the bump valley. This means that the passive by-pass jet in the passive jet bump exerts stronger effect in reducing the strength of the reverse flow in the wake region than that caused by the injection of the 1 bar total pressure jet in the valley of the active jet bump at $x/h = 6$. In contrast, at the normalised x-location $x/h = 7$ (Fig. 11(b)), the x-velocity in the wake region of the passive jet bump becomes similar to that of the plain bump and the active jet bump without jet blowing. This indicates that the passive by-pass jet in the passive jet bump provides very little influence in affecting the wake flow at any normalised location downstream of $x/h = 6$. In addition, from Fig. 11(b), it can be seen that at the normalised location

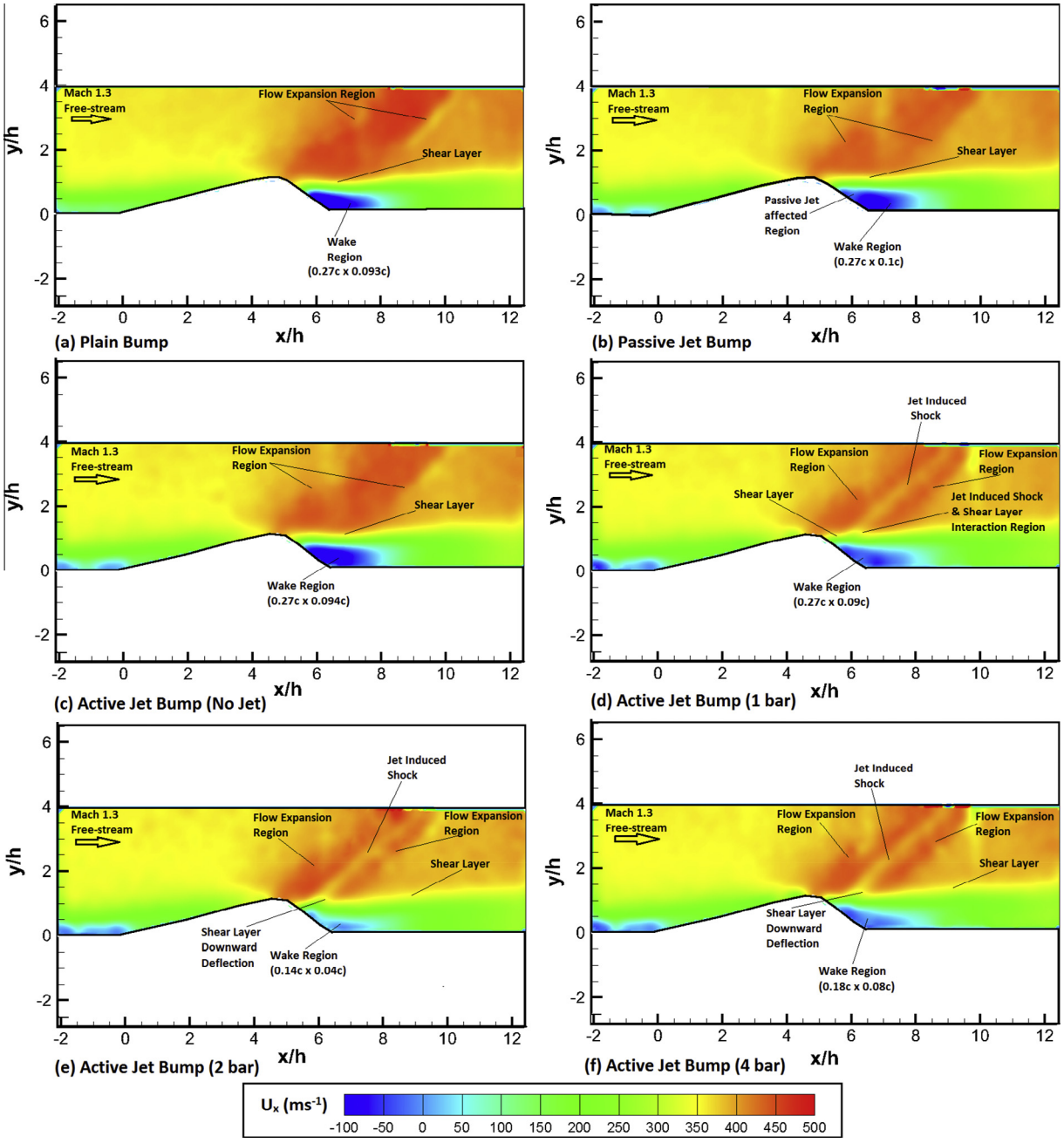

Fig. 10. The x-velocity contours along the centreline of (a) Plain bump, (b) passive jet bump, (c) active jet bump with no jet blowing, (d) to (f) active jet bump with 1, 2 and 4 bar total pressure sonic jet blowing in the bump valley, respectively.

x/h = 7, the x-velocity in the wake region of the active jet bump is the highest when 2 bar total pressure jet is blowing in the bump valley, followed by the injection of the 4 and 1 bar total pressure jet. In fact, no or only weak reverse flow appears in the wake region of the active jet bump at this normalised x-location when 2 and 4 bar total pressure jet is blowing in the bump valley.

To summarise the results shown in Figs. 10 and 11, it is clear that the size and strength of the wake region of the rounded contour bumps could be reduced by blowing jet in the bump valley. It is observed that blowing active jet with 2 bar jet total pressure shows the highest effectiveness in achieving wake flow control followed by injecting 4 and 1 bar total pressure jet. Passive by-pass jet could only influence the strength of the reverse flow in the wake region near the location where the jet orifices are situated. It is deduced that the blowing jet, either active or passive, increases the momentum of the flow in the wake region. As a result, flow reversal in the wake region is more difficult to happen when jet is injected in the valley of the contour bump.

For the size reduction effect of the wake region, a hypothesis is made here in attempt to relate the influence of the active blowing jet in the bump valley with the flow pattern downstream of the bump crest of the active jet bump. In fact, by observing Fig. 10 (c), an interesting phenomenon can be observed when the 2 bar total pressure jet is blowing in the valley of the active jet bump. As previously mentioned that a small region which shows abrupt x-velocity reduction appears immediately downstream of the bump crest caused by the presence of the jet induced shock there. A closer examination to that small region reveals that the flow in

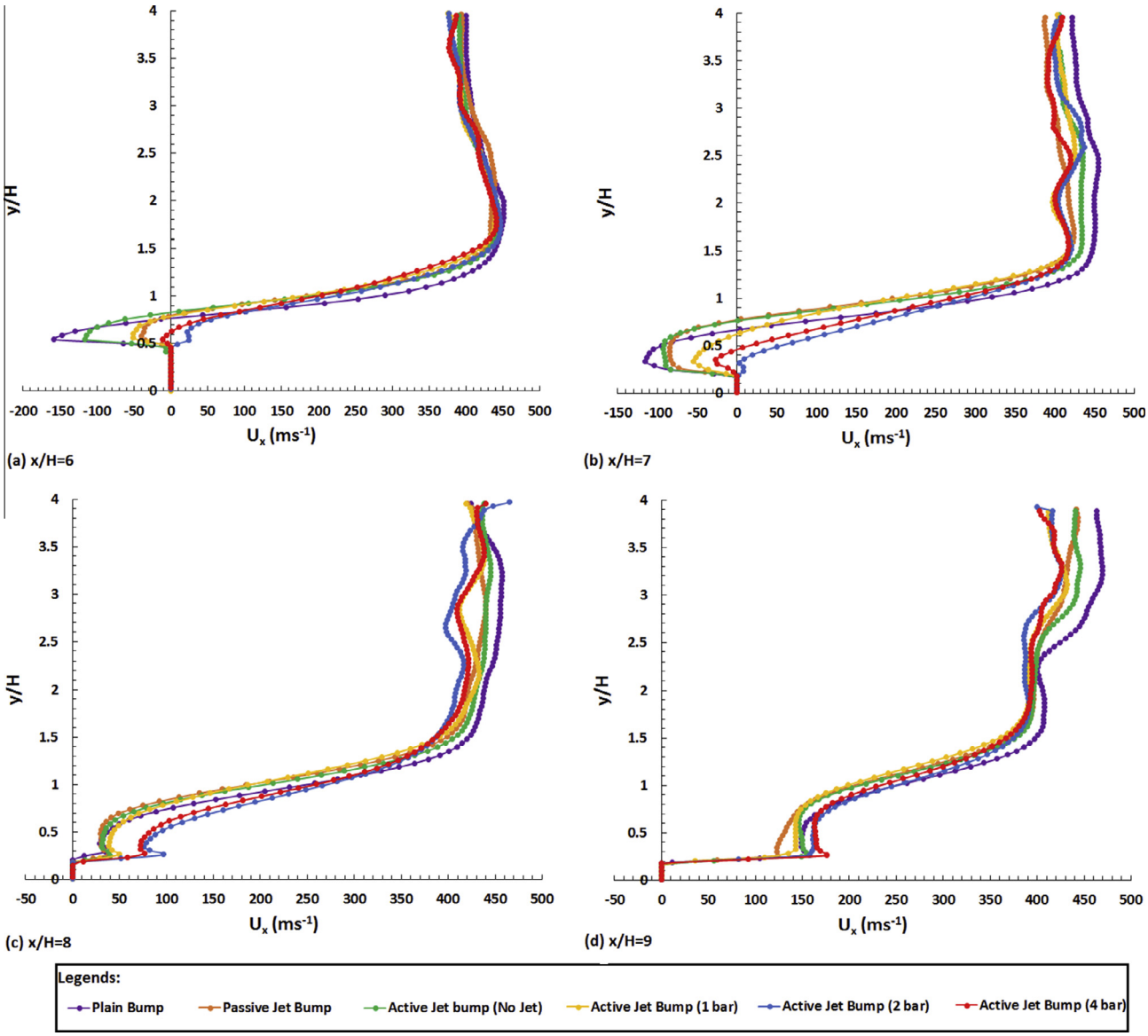

Fig. 11. The x-velocity profiles of different rounded contour bumps being studied measured at the normalised locations: (a) x/h = 6, (b) x/h = 7, (c) x/h = 8 and (d) x/h = 9 in the wake region.

the shear layer was deflected strongly downwards across the jet induced shock. To be exact, it is deduced that the flow downstream of the bump crest of the active jet bump with 2 bar total pressure jet blowing shows stronger downwards motion than that shown along the valley of the plain bump (Fig. 10(a)). Therefore, the separated flow downstream of the bump crest is quickly reattached in the present case when 2 bar total pressure jet is injected in the bump valley. As a result, only a small wake region is formed downstream of the bump crest in the present case. In fact, similar but weaker shear layer deflection pattern could also be observed when 1 and 4 bar total pressure jet is blowing in the valley of the active jet bump shown in Fig. 10(d) and (f), respectively. This explains why the wake region is the smallest when 2 bar total pressure jet is blowing in the valley of the active jet bump compared to the size of the wake region that presented in any other rounded contour bumps being studied.

In fact, the hypothesis made here to explain the formation of the smaller recirculating flow region in the bump valley with active jet injected into the flow field is supported by considering the time-averaged y-velocity contours of different contour bumps being studied as shown in Fig. 12.

The time-averaged y-velocity contour of the plain bump is shown in Fig. 12(a). The presence of the ramp-shaped front surface of the plain bump means that strong upwards flow movement appears upstream of the bump crest. Therefore, a region that shows high positive y-velocity occurs along the front face of the plain bump as seen in Fig. 12(a). At the bump crest, the expansion waves that present there progressively changes the flow direction from upwards to slightly downwards. Therefore, the flow immediately downstream of the bump crest shows moderate level of downwards motion. However, due to the continuous flow compression effect along the concave-shaped bump valley, another region that shows strong upwards flow motion appears at the middle of the bump valley. The presence of this upward flow movement region delays the reattachment of the separated flow downstream of the bump crest. This explains why a large wake region is shown downstream of the bump crest of the plain bump. Similar time-averaged y-velocity contours could also be observed

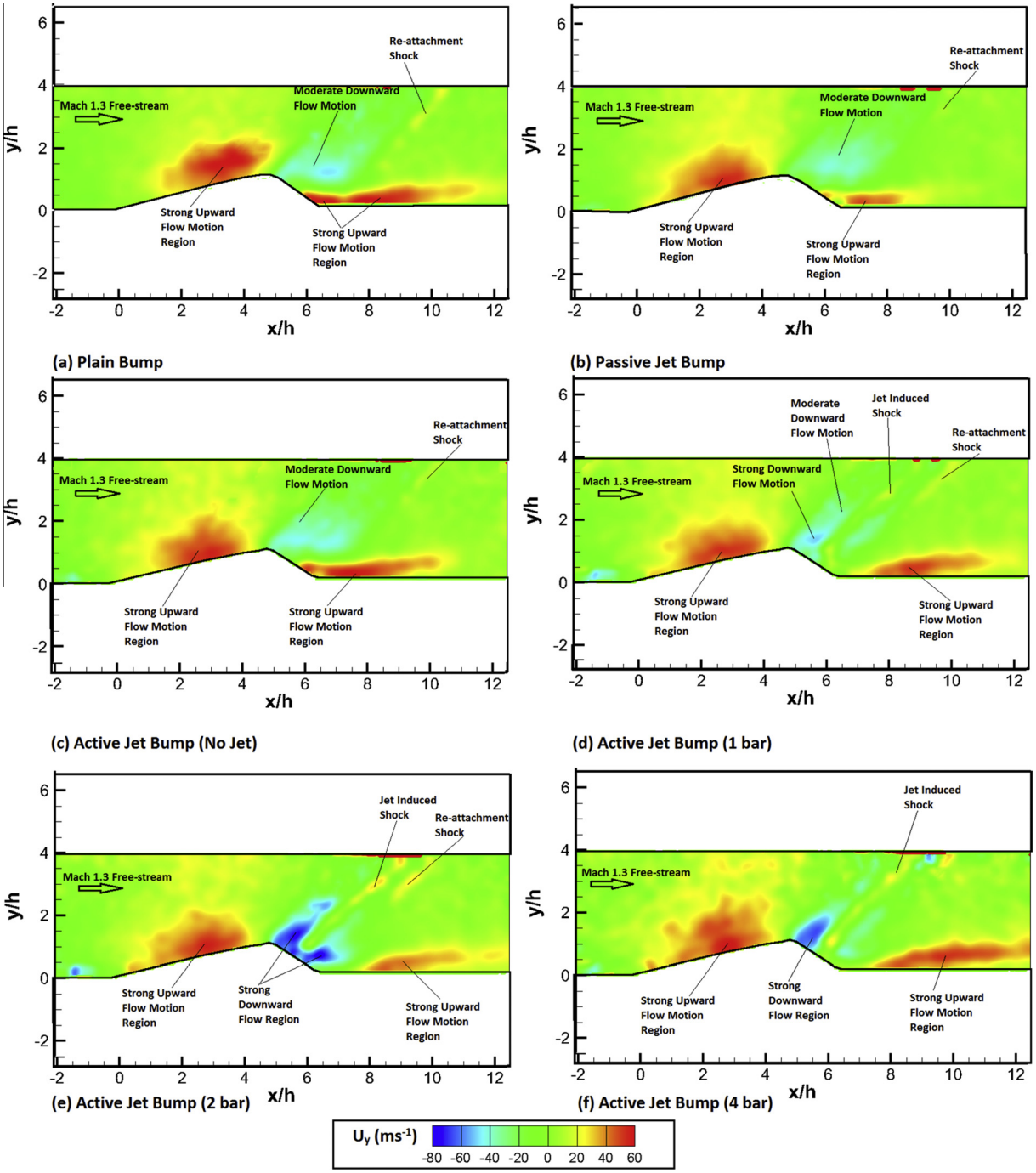

Fig. 12. The y-velocity contours along the centreline of (a) Plain bump, (b) passive jet bump, (c) active jet bump with no jet blowing, (d) to (f) active jet bump with 1, 2 and 4 bar total pressure sonic jet blowing in the bump valley, respectively.

in the passive jet bump (Fig. 12(b)) and the active jet bump without jet blowing employed (Fig. 12(c)) although in the former case the strength of the positive y-velocity region at the middle of the bump valley is slightly weaker.

Dramatic changes appear when jet is blowing in the valley of the active jet bump as shown in Fig. 12(d)–(f). Firstly, from Fig. 12(d)–(f), it can be seen that when active jet is blowing in the bump valley, the region that shows strong upwards flow motion downstream of the bump crest is shifted from the middle of the bump valley as in the case of the plain bump (Fig. 12(a)) to somewhere downstream of the rear end of the bump. Secondly, from Fig. 12(e), it can be seen that two considerably large regions that show highly negative y-velocity appear along the valley of the active jet bump when 2 bar total pressure jet is injected. This indicated that the flow downstream of the bump crest shows strong downwards motion in this case. This supports the hypothesis made earlier that the flow was deflected downwards by the jet induced shock and it explains why the smallest recirculating flow region is formed downstream of the bump crest when 2 bar total pressure jet is injected in the valley of the active jet bump. In fact, a similar region that shows considerably strong downwards flow movement is also shown immediately downstream of the bump valley in the case when the total pressure of the blowing jet is 4 bar (Fig. 12(f)). However, the size and strength of this strong downwards flow

motion region in this case is smaller and weaker than that shown when 2 bar total pressure jet is used. This explains why the size of the wake region that formed when 4 bar total pressure jet is injected is slightly larger than that when 2 bar total pressure jet is injected in the valley of the active jet bump. Nevertheless, the results shown in Fig. 12 indicate that the jet induced shock that present in the valley of the active jet bump when jet is injected in the bump valley deflects the flow downwards so that a smaller recirculating flow region is formed in the bump valley.

5. Conclusions

An experimental study has been conducted to investigate the flow pattern over various three-dimensional rounded contour bumps in a Mach 1.3 supersonic freestream using an in-draft supersonic wind tunnel. Totally three rounded contour bumps known as the plain bump, the passive jet bump and the active jet bump, were used. In the active jet bump sonic jet with total pressure ranging from 0 to 4 bar was injected continuously in the bump valley in attempt to achieve flow control downstream of the bump crest. Surface oil flow visualisation, Schlieren photography technique and two-component time-averaged particle image velocimetry measurements were used for flow diagnostics.

Experimental data showed that when the Mach 1.3 freestream flew over the baseline plain bump, the occurrence of flow separation downstream of the bump crest led to the formation of a large wake region downstream. In addition, the presence of this low pressure wake region attracted the flow around the bump from the two sides to flow into and circulated in the bump valley. As a result, two large spanwise counter-rotating vortices were formed in the bump valley. It was concluded that the general spanwise flow pattern over the plain bump in a Mach 1.3 freestream is similar to that shown when a Mach 1.9 supersonic freestream is used. However, it was observed that the size of the spanwise vortices that formed in the present case was larger than those shown in a Mach 1.9 freestream.

For the effects of the passive by-pass jet in achieving flow control in the passive jet bump, it was shown in the surface oil flow visualisation image that the passive jet could distort the spanwise vortices that formed in the bump valley. The spanwise vortices that present in the valley of the passive jet bump were highly diffused although their sizes were similar to those shown in the plain bump. It was concluded that the passive by-pass jet could exert certain effect in distorting the vortex cores of the spanwise vortices. In contrast, the passive by-pass jet blowing in the valley of the passive jet bump could not reduce the size of the wake region that formed downstream of the bump crest although it could reduce the strength of the reverse flow in the wake region at the normalised x-location $x/h = 6$. However, it was observed that this reverse flow weakening effect diminished quickly and basically showed no effect at any normalised x-location from $x/h = 7$ onwards.

In the active jet bump, the experimental data obtained show that when no jet is blowing in the bump valley, the spanwise and streamwise flow pattern appeared over the bump were similar to those shown in the plain bump. In fact, the sizes of the wake region and the spanwise vortices that formed in the valley of the active jet bump without jet blowing employed were resembled to those shown in the plain bump. Therefore, it is concluded that the active jet bump could be considered as a plain bump when no jet is blowing in the valley of the bump. Changes started to appear in term of the spanwise flow pattern over the active jet bump when jet is blowing in the bump valley. In general, it was observed that the blowing jet could always distort the spanwise vortices that formed in the bump valley. In addition, it was found that the size of the spanwise vortices could also be reduced by the blowing jet when the jet total pressure is set to 2 bar or above. It was concluded that the smallest spanwise vortices were formed when 2 bar total pressure jet was injected into the flow field. It is believed that the blowing jet in the valley of the active jet bump increased the local pressure level around the centre portion of the bump valley. Therefore, less flow from the two sides of the bump was attracted to circulate in the bump valley and consequently led to the formation of the smaller spanwise vortices. It is deduced that, in general, the injection of high total pressure jet exhibits influence to a greater area in the bump valley. As a result, in general, the size of the spanwise vortices that formed in the valley of the active jet bump decreases with increasing the total pressure of the injected jet.

For the streamwise flow pattern over the active jet bump with jet blowing in the bump valley, from the Schlieren photography images obtained, it was observed that the incoming flow downstream of the bump crest interacted with the injected jet and led to the formation of the jet induced shock in the bump valley. The strength of the jet induced shock, in general, increased with increasing the total pressure of the blowing jet. In addition, it was observed that the jet induced shock could deflect the shear layer downwards and hence, reduce the size of the wake region that shown downstream of the bump crest. It was concluded that the shear layer pointed the most downwards when 2 bar total pressure jet was injected in the valley of the active jet bump, followed by the case when total pressure of the jet was 4 bar. In fact, the data obtained from the particle image velocimetry measurements concluded that the blowing jet in the valley of the active jet bump could reduce the size and strength of the wake region. It was found that this flow separation control measure is the most effective when the total pressure of the blowing jet is 2 bar, followed by 4 bar. It is clear that in these two cases, the size of the wake region and the strength of the reverse flow in the wake region were significantly reduced by the effect of the injected jet. It is deduced that the blowing jet increases the momentum of the flow and hence flow reversal becomes more difficult to occur in the wake region particularly when blowing jet with high total pressure is injected.

Finally, a hypothesis was proposed in attempt to explain the relation between the size of the wake region that formed in the bump valley of the active jet bump and the total pressure of the blowing jet. It was observed that the jet induced shock that presented in the bump valley defected the flow downstream of the bump crest downwards. As a result, the separated flow downstream of the bump crest of the active jet bump was quickly re-attached and hence, a smaller wake region was formed in those cases when jet was injected in the valley of the active jet bump.

Author contributions

All experiments, data processing and analysis were conducted by Kin Hing Lo. Manuscript preparation and editing were conducted by both Kin Hing Lo and Konstantinos Kontis.

Conflicts of interest

The authors declare no conflict of interest.

Acknowledgments

The authors would like to acknowledge Prof. Ning Qin in the University of Sheffield for providing the geometry and design parameters of the optimised three-dimensional rounded contour bump used in the present experimental study. In addition, the

authors would like to acknowledge the Engineering and Physical Sciences Research Council (EPSRC) – United Kingdom for funding this research (EPSRC award no.: EPSRC EP/K504488/1).

References

[1] J.P. Eastwood, J.P. Jarrett, Toward designing with three-dimensional bumps for lift/drag improvement and buffet alleviation, AIAA J. 50 (12) (2012) 2882–2898.

[2] B. König, M. Pätzold, T. Lutz, E. Krämer, Shock control bumps on flexible and trimmed transport aircraft in Transonic Flow, New Results in Numerical and Experimental Fluid Mechanics VI, Notes on Numerical Fluid Mechanics and Multidisciplinary Design (NNFM), vol. 96, 2007, pp. 80–87.

[3] B. König, M. Pätzold, T. Lutz, E. Krämer, H. Rosemann, K. Richter, H. Uhlemann, Numerical and experimental validation of three-dimensional shock control bumps, J. Aircraft 46 (2) (2009) 675–682.

[4] N. Qin, W.S. Wong, A. Le Moigne, Three-dimensional contour bumps for transonic wing drag reduction, Proc. IMech E Part G J. Aerosp. Eng. 222 (5) (2008) 619–629.

[5] W.S. Wong, N. Qin, N. Sellars, H. Holden, H. Babinsky, A combined experimental and numerical study of flow structures over three-dimensional shock control bumps, J. Aerosp. Sci. Technol. 12 (2008) 436–447.

[6] K.H. Lo, H. Zare-Behtash, M. Johnson, K. Kontis, Control of flow separation on a contour bump by jets: an experimental study, in: Proceedings of the 29th International Symposium on Shock Waves, Madison, United States, July 14–19 2013, 2013.

[7] P.J.K. Bruce, S.P. Colliss, Review of research into shock control bumps, Shock Waves 25 (5) (2015) 451–471.

[8] S.P. Colliss, H. Babinsky, K. Nübler, T. Lutz, Joint experimental and numerical approach to three-dimensional shock control bump research, AIAA J. 52 (2) (2014) 436–446.

[9] G. Byun, C. Long, R. Simpson, Study of vortical separation from three-dimensional symmetric bumps, AIAA J. 42 (4) (2004) 754–765.

[10] A. Yakeno, S. Kawai, T. Nonomura, K. Fujii, Separation control based on turbulence transition around a two-dimensional hump at different Reynolds numbers, Int. J. Heat Fluid Flow 55 (2015) 52–64.

[11] G. Iaccarino, C. Marongiu, P. Catalano, M. Amato, RANS simulation of the separated flow over a bump with active control Annual Research Briefs, Centre for Turbulence Research, 2003, pp. 389–397.

[12] M. Svensson, A CFD investigation of a generic bump and its application to a diverterless supersonic inlet Master Thesis, Linkoping University, Linkoping Sweden, 2013.

[13] K.H. Lo, Experimental studies on contour bumps and cavities at supersonic speed PhD Thesis, University of Manchester, Manchester, United Kingdom, 2014.

[14] K.H. Lo, H. Zare-Behtash, K. Kontis, Control of flow separation on a contour bump by jets in a Mach 1.9 freestream: an experimental study, Acta Astronaut. 126 (2016) 229–242.

[15] S. Koike, K. Suzuki, E. Kitamura, M. Hirota, K. Takita, G. Masuya, M. Matsumoto, Measurement of vortices and shock waves produced by ramp and twin jets, J. Propul. Power 22 (2006) 1059–1067.

[16] A.I. Zubkov, A.I. Glagolev, Yu.A. Panov, Injection of gaseous jets in supersonic flow from orifices located on a side wall of a flying body, Mosc. Univ. Mech. Bull., Ser. 1 Mathe., Mech. 5 (1968) 66–72.

[17] K. Kontis, J.L. Stollery, Control effectiveness of a jet-slender body combination at hypersonic speeds, J. Spacecraft Rockets 34 (6) (1997) 762–768.

[18] N. Qin, Y. Zhu, S.T. Shaw, Numerical study of active shock control for transonic aerodynamics, Numer. Methods Heat Fluid Flow 14 (2004) 444–466.

[19] Y. Zhu, Computational study of shock control at transonic speed PhD Thesis, College of Aeronautics, Cranfield University, Cranfield, United Kingdom, 2000.

[20] Y. Zhu, N. Qin, Inclined slot blowing on transonic aerodynamics performance of the RAE 5243 and RAE 5225 aerofoils CoA Report 9906, Cranfield University, United Kingdom, 1999.

[21] W.F. Wong, Application of boundary layer blowing to suppress strong shock induced separation in supersonic inlet, AIAA J. (1977) 77–147.

[22] T. Ukai, H. Zare-Behtash, K.H. Lo, K. Kontis, S. Obayashi, Effectiveness of dual jets distance on mixing characteristics and flow path within a cavity in supersonic cross flow, Int. J. Heat Fluid Flow 50 (2014) 254–262.

[23] T. Ukai, H. Zare-Behtash, E. Erdem, K.H. Lo, K. Kontis, S. Obayashi, Effectiveness of jet location on mixing characteristics inside a cavity in supersonic flow, Exp. Therm. Fluid Sci. 52 (2014) 59–67.

[24] H. Zare-Behtash, K.H. Lo, K. Kontis, T. Ukai, S. Obayashi, Transverse jet-cavity interactions with the influence of an impinging shock, Int J. Heat Fluid Flow 53 (2015) 146–155.

[25] K.H. Lo, K. Kontis, Static and wind-on performance of polymer-based pressure sensitive paints using platinum and ruthenium as the luminophore, Sensors 16 (5) (2016) 595.

[26] K.H. Lo, H. Zare-Behtash, K. Kontis, Flow characteristics along an active jets equipped contour bump in a supersonic freestream and its potential to be applied on transonic aircraft for drag reduction: an experimental study, in: Proceedings of 53rd AIAA Aerospace Sciences Meeting, Kissimmee, FL, USA, 5–9 January 2015, 2015.

[27] H. Zare-Behtash, K.H. Lo, L. Yang, K. Kontis, Pressure sensitive paint measurements at high Mach numbers, Flow Meas. Instrum. (2016), http://dx.doi.org/10.1016/j.flowmeasinst.2016.02.004 (in press).

[28] M.R. Saad, H. Zare-Behtash, A. Che-Idris, K. Kontis, Micro-ramps for hypersonic flow control, Micromachines 3 (2) (2012) 364–378.

[29] L. Yang, H. Zare-Behtash, E. Erdem, K. Kontis, Application of AA-PSP to hypersonic flows: the double ramp model, Sens. Actuators B: Chem. 161 (2012) 100–107.

[30] H. Zare-Behtash, N. Gongora-Orozco, K. Kontis, S.J. Holder, Application of novel pressure-sensitive paint formulations for the surface flow mapping of high-speed jets, Exp. Thermal Fluid Sci. 33 (5) (2009) 852–864.

[31] N. Gongora-Orozco, H. Zare-Behtash, K. Kontis, Global unsteady pressure-sensitive paint measurements of a moving shock wave using thin-layer chromatography, Measurement 43 (1) (2010) 152–155.

[32] M.K. Quinn, L. Yang, K. Kontis, Pressure-sensitive paint: effect of substrate, Sensors 11 (12) (2011) 11649–11663.

[33] L. Yang, E. Erdem, H. Zare-Behtash, K. Kontis, S. Saravanan, Pressure-sensitive paint on a truncated cone in hypersonic flow at incidences, Int. J. Heat Fluid Flow 37 (2012) 9–21.

[34] L. Yang, H. Zare-Behtash, E. Erdem, K. Kontis, Investigation of the double ramp in hypersonic flow using luminescent measurement systems, Exp. Thermal Fluid Sci. 40 (2012) 50–56.

[35] N. Gongora-Orozco, H. Zare-Behtash, K. Kontis, Effects of filters on the performance and characteristics of pressure-sensitive paints, Meas. Sci. Technol. 20 (7) (2009) 077004.

[36] M.K. Quinn, N. Gongora-Orozco, K. Kontis, P. Ireland, Application of pressure-sensitive paint to low-speed flow around a U-bend of strong curvature, Exp. Thermal Fluid Sci. 48 (2013) 58–66.

[37] H. Zare-Behtash, N. Gongora-Orozco, K. Kontis, PSP visualisation studies on a convergent nozzle with an ejector system, J. Visualization 12 (2) (2009) 157–163.

[38] J.W. Bradley, J.S. Oh, O.T. Olabanji, C. Hale, R. Mariani, K. Kontis, Schlieren photography of the outflow from a plasma jet, IEEE Trans. Plasma Sci. 39 (11) (2011) 2312–2313.

[39] K. Kontis, A review of some current research on pressure-sensitive paint and thermographic phosphor techniques, Aeronaut. J. 111 (1122) (2007) 495–508.

[40] K. Kontis, Y. Syogenji, N. Yoshikawa, Surface thermometry by laser-induced fluorescence of Dy^{3+}:YAG, Aeronaut. J. 106 (1062) (2002) 453–457.

[41] E. Erdem, K. Kontis, Numerical and experimental investigation of transverse injection flows, Shock Waves 20 (2) (2010) 103–118.

[42] W.T. Lusk, Control of supersonic cavity flow by leading edge blowing Master Thesis, University of Florida, United States, 2011.

[43] T. Lusk, J. Dudley, L. Ukeiley, L. Cattafesta, Flow field effects on control on supersonic open cavities, in: Proceedings of 49th AIAA Aerospace Sciences Meeting Including the New Horizons Forum and Aerospace Exposition, Orlando, Florida, United States, 4–7 January, 2011, 2011.

[44] T. Lusk, L. Cattafesta, L. Ukeiley, Leading edge slot blowing on an open cavity in supersonic flow, Exp. Fluid 53 (2012) 187–199.